Exploring the morphology of flax fibres by X-ray microtomography and the related mechanical response by numerical modelling

E. Richely, A. Bourmaud, H. Dhakal, Z. Zhang, Johnny Beaugrand, S. Guessasma

Exploring the morphology of flax fibres by X-ray microtomography and the related mechanical response by numerical modelling

E. Richely[1], A. Bourmaud[2], H. Dhakal[3], Z. Zhang[3], J. Beaugrand[1] and S. Guessasma[1]*

[1] UR1268 BIA. INRAE Nantes. BP 71627. 44316 Nantes Cedex 03, France

[2] Univ. Bretagne Sud, UMR CNRS 6027, IRDL, Lorient, France

[3] Advanced Polymer and Composites (APC) Research Group, University of Portsmouth, Hampshire PO1 3DJ, United Kingdom

*Correspondence: sofiane.guessasma@inrae.fr Tel.: +33-(0)240675036

Abstract

The external shape and internal lumen of flax fibres are investigated using X-ray microtomography (µ-CT) and finite element (FE) modelling. µ-CT reveals an intricate flax fibre and lumen morphology, with mean porosity contents between 0 and 7.2%. The FE model is based on 3D volumes obtained by X-ray µ-CT and tensile testing in the elastic domain. Numerical results demonstrate the decrease of stiffness as a combined effect of porosity and stress heterogeneity triggered by geometrical considerations. Moreover, stress concentrations induced by both surface roughness and complex lumen shape were observed, highlighting their possible implication in failure mechanisms. However, Young's moduli are overestimated compared to experimental curves and non-linearities are not considered by the rather strong hypothesis of this model (linear elastic material: no viscosity, plasticity or damage mechanisms taken into account). Future work should include the orientation and

reorientation of cellulose microfibrils upon tensile testing, as well as damage mechanisms.

Keywords: Natural fibers, Stress concentrations, Finite element analysis, X-ray microtomography

1. Introduction

In the present context of growing demand for sustainable resources, plant fibres have gained increasing visibility and hold on the market in recent years, as an alternative to synthetic fibres such as glass fibres. Indeed, the Nova Institute reported a European production of biocomposites of 480,000 tonnes in 2020 [1], among which bast fibres represented 9%. Between plant fibres, flax appears as a promising candidate, with environmental advantages compared to glass fibres which have already been confirmed by life cycle assessment [2]. However, its use at a larger scale for semi-structural products is undermined by several factors, such as the difficulty of predicting the quality and thus ensure the reproducibility of its mechanical performances. Indeed, the natural character of plant fibres introduces variabilities at different levels, imposing great challenges to better understand their structure-mechanical property relationship. A distinctive characteristic of most plant fibres compared to glass fibres is the presence of a higher dispersion in terms of morphology [3, 4]. However, observations are often based on cross-sectional views at a single location along a fibre. For instance, Mattrand et al. [5] modelled the scatter in flax fibre and bundle cross-sections based on observation of hundreds of flax fibre and bundle cross-sections, providing an efficient tool for future modelling but not taking into account the variability of cross-section along the fibres. Moreover, most plant fibres present a porous structure composed of a main intrinsic porosity called lumen, which is filled with cellular material during the cell life and emptied after the demise of the plant [6, 7], as well as smaller internal cavities of a few μm in diameter [8-10]. Regarding the lumen size of flax,

2

mean values ranging from 1.6 % to 6.8 ± 3.5 % can be found in literature [3, 6, 11], highlighting intra-fibre variabilities. As for external boundaries such measurements are often based on cross-sectional observations of fibres or stems embedded in a resin and further image processing, not reflecting the possible evolutions along a fibre. Nevertheless, due to the small size of the fibres and related experimental difficulties, few studies evidenced the variations of the lumen and external boundaries along some flax and hemp fibres thanks to X-ray microtomography (µ-CT) [12-14]. In particular, a previous experimental work developed by the co-authors [14] reported mean porosity contents between 0.4 and 7.3 % with high variabilities along the different fibres investigated, leading to a hypothesized failure scenario under tension involving interactions between the defects and intricate lumen size along the fibres. At the composite scale, the central lumen has been depicted as a preferential site of crack initiation in flax composites [15], possibly due to the creation of stress concentration. A better understanding of the mechanisms at stake requires an investigation of the consequences of flax intricate morphology on the mechanical properties at the fibre scale, which involves complex experimental set-ups. With this in view, *in situ* tensile testing combined to Synchrotron X-ray µ-CT was undertaken by Beaugrand et al. on hemp [12], highlighting a broad range of damage mechanisms involving porosity. However, the failure initiation was not addressed as the samples were initially notched. Other failure scenarios at the fibre scale are often based on *post mortem* observations [8, 16], only giving partial information on failure initiation and propagation. In this context, numerical modelling emerged from the wood area a few decades ago as a powerful and complementary tool to decipher the mechanical behaviour of plant fibres [17]. A few authors investigated the link between the morphology and mechanical properties of different plant fibres. In particular, Gassan et al. [18] compared two elastic models and evidenced an overestimation of the elastic modulus of approximately 30% when considering an elliptical structure. The influence of the 3D geometry of hemp fibres on their tensile behaviours was further investigated in a model

3

developed by Del Masto et al. [19], showing a strong influence of the degree of ellipticity on the shape of the nonlinear response. In this study, the variation in cross-section along the fibres was not considered and simplified outlines of the fibres were used since both exhibited a minor influence on the shape of the tensile response. However, these parameters should not be neglected when investigating the failure mechanisms since they might induce stress concentrations.

Therefore, the present work is aiming at deciphering the consequences of the flax fibre intricate morphology on its mechanical properties. To achieve this, the finite element method was applied on the precisely described fibre volume obtained by X-ray μ-CT in order to access global properties such as Young's modulus, as well as local stress and strain distributions induced by the intricate fibre shapes. The general approach is summarized in **Figure 1**.

2. Experimental characterization

2.1. Materials

Textile flax fibres *(Linum usitatissimum)* from the Bolchoï variety were provided by Groupe Depestele / Teillage Vandecandelaère (Bourguebus, France). The plants were cultivated in Normandy (France) in 2017. Fibre extraction was achieved by industrial scutching after a step of dew-retting in the field. In addition, two fibres from the Marylin and Drakkar varieties (textile flax fibres varieties) and cultivated in 2016 and 2012 respectively, have been used for the X-ray μ-CT experiments and included in the numerical study because providing contrasted geometries whose mechanical responses to numerical simulation appeared interesting.

2.2. X-ray microtomography

X-ray μ-CT was performed using a Xradia 510 Versa tomograph (Zeiss, Marly-le-Roi, France). A voxel size as small as 150 nm was reached, and scans were acquired for 4 unitary flax fibres (*a*, *b*, *c* and *d*). Image processing was conducted on resulting scans using the software FIJI

(https://fiji.sc/) and the plugin Morpholibj developed by Legland et al. [20]. More details about the experimental and image processing parameters can be found in [14]. The aspect ratio is defined as the ratio between the major and minor axis of the particle's fitted ellipse. The aspect ratio is here calculated on transversal cross-sections of fibres and should not be confused with the aspect ratio of short fibres commonly depicted as their length over the diameter. The porosity content is obtained for each fibre transverse cross-section as follows:

$$\text{porosity (\%)} = 100 * \frac{\Sigma\, V_p}{\Sigma\, V_f} \qquad (1)$$

where, for each cross-section, V_p represents the voxels corresponding to porosity and V_f the voxels corresponding to the filled fibre. At a macroscopic scale, the mean porosity content is calculated as the average value of the cross-sectional porosities along the fibre considered.

2.3. Tensile testing

Tensile testing experiments were carried out on 42 unitary fibres from the Bolchoï variety in a MTS machine (MTS System, Créteil, France), operating with a 2N load cell and a displacement rate of 1 mm/min, following the norm AFNOR NF T 25-501. The controlled testing environment was set to $25 \pm 1°C$ and 48 ± 2 % of relative humidity. The fibres were extracted manually and further glued on a paper frame with a gauge length of 10 mm. The cross-sectional areas S were determined using a circular idealization, using the following equation:

$$S = \Pi * \left(\frac{d}{2}\right)^2 \qquad (2)$$

with d the mean diameter assessed from 6 measurements along each fibre using an optical microscope (Leitz DMRB, Leica Microsystems, Nanterre, France) equipped with a Hamamatsu digital camera (C11440 ORCA-Flash4.0 LT). The compliance of the system was considered for the correction of the cross-head displacement, following the NF T25-501-3 standard. Regarding the strain measurements, they are based on the cross-head displacements following the existing standard for tensile testing of plant fibres AFNOR NF T 25-501 and we can not exclude

drawbacks from the strain measurement method, however it is very difficult to use extensometer or DIC methods due to the small size of the fibres (mean diameters between 10 and 25 μm). Moreover, the stiffness was calculated in the last linear part of each stress-strain curve, following the AFNOR standard NF T25-501-3.

3. Numerical model

3.1. Geometry and meshing

The binarized images from X-ray μ-CT forming the 3D volumes of the fibres were directly meshed using the software Simpleware ScanIP. As the close X-ray absorption properties of the different flax fibre sublayers and the very thin thickness of the external layers did not permit their differentiation upon X-ray μ-CT, the fibres were considered only made of the main G-layer, which constitute the thicker cell wall [21, 22]. The meshing elements were tetrahedrons of the second order (serendipity elements, quadratic discretization), with 3 degrees of freedom (dof) at each node corresponding to the displacements in the x, y and z directions. A convergence analysis was performed in order to find the best compromise in terms of calculation time / accuracy of the result. The meshing coarseness and voxel size of fibre **a** was varied, leading to a number of dof between 1.1×10^5 and 6.3×10^6, and a mean element volume between 325×10^{-3} and 5×10^{-3} μm^3. The accuracy of the results was evaluated based on both the error in overall stiffness and stress profiles. A cross-sectional view of the meshing, resulting axial stress σ_{33} in the tensile direction and Young's modulus as a function of the dof can be found in **Figure 2**. In order to accurately represent the porosity content of the fibre and therefore the resulting Young's modulus, as well as a sufficient resolution to capture stress concentrations induced by the surface roughness and lumen intricate shape, the third meshing coarseness was applied to all fibres, leading to model sizes between 9.10^5 and 5.10^6 dof.

Moreover, fibres based on the extrusion of the cross-section at one extremity of each volume from X-ray tomography were used as a comparison, with no variation of cross-section along their length (-NV). Finally, both fibre types were artificially "filled" by image processing (i.e. the internal porosities were removed) using the "fill holes" function of FIJI software, and used as a comparison to assess the influence of the lumen (-F and -NV-F). In addition to involving *real* fibres, computations are performed on *fibre models*. These are cylindrical fibres with a diameter of 15 μm and a varying lumen content from 0 to 10%. The fibre models were created and meshed directly on Comsol software, in order to compare the results and better highlight the consequences of the intricate lumen shapes evidenced by X-ray μ-CT. For the meshing, the same minimum and maximum element length as defined for fibres meshed with Simpleware ScanIP were implemented.

The length of the fibre with no lumen was varied between 50 μm and 10 mm to assess the influence of the same boundary conditions with different fibre lengths on Young's modulus (**Figure 3a**). The difference in predicted Young's modulus is negligible between a fibre of 140 μm in length and a 10 mm fibre, the reference length for experimental tensile testing following the norm AFNOR NF T 25-501. Moreover, as observed in **Figure 3b**, stress concentrations induced by the boundary conditions impact less than 10% of the total fibre length. Lengths of 140 μm will therefore be chosen for the rest of the study in order to establish comparison with the fibres from X-ray μ-CT whose scanned lengths are close to 140 μm. The different fibre geometries and related parameters are summarized in **Table 1**.

3.2. Constitutive law

The main parameters of the finite element analysis (FEA) used in this chapter are summarized in **Figure 4**. In this first model, the material was considered as linear elastic, neglecting viscous and plastic behaviours. Therefore, it follows Hooke's law:

$$[\sigma] = [S^\varepsilon]^{-1} * [\varepsilon] \text{ and } [\varepsilon] = [S^\varepsilon] * [\sigma] \qquad (3)$$

where σ is the stress tensor (3x3), ε is the strain tensor (3x3) and S^ε the tensor of compliance, a

6x6 symmetric matrix containing a maximum of 21 independent parameters for an anisotropic

material. In the coordinate system related to the cellulose microfibrils, the fibre cell wall can be

seen as a transversely isotropic material, with an axis of symmetry in the direction of the

microfibrils. Therefore, the elastic compliance tensor can be simplified into the following form:

$$[S^\varepsilon] = \begin{bmatrix} \frac{1}{E_T} & -\frac{v_{TT}}{E_T} & -\frac{v_{TL}}{E_T} & 0 & 0 & 0 \\ -\frac{v_{TT}}{E_T} & \frac{1}{E_T} & -\frac{v_{TL}}{E_T} & 0 & 0 & 0 \\ -\frac{v_{LT}}{E_L} & -\frac{v_{LT}}{E_L} & \frac{1}{E_L} & 0 & 0 & 0 \\ 0 & 0 & 0 & \frac{1}{G_{LT}} & 0 & 0 \\ 0 & 0 & 0 & 0 & \frac{1}{G_{LT}} & 0 \\ 0 & 0 & 0 & 0 & 0 & \frac{1}{G_{TT}} \end{bmatrix} \qquad (4)$$

The compliance tensor is expressed in the coordinate system related to the microfibrils

represented in **Figure 4**, which correspond to the global coordinate system under the

assumption of a MFA equal to 0. E_L and E_T are referring to the longitudinal and transverse

Young's modulus of the cell wall, G_{LT} and G_{TT} are shear moduli and v_{TT}, v_{TL}, v_{LT} are Poisson's

coefficients. The symmetry of the compliance matrix and the following equation induced by the

transverse isotropy permit to reduce the number of independent variables to 5:

$$G_{TT} = \frac{E_T}{2*(1+v_{TT})} \qquad (5)$$

The material inputs were chosen in agreement with experimentally determined cellulose

content and crystallinity for the same flax variety obtained by biochemical analysis and solid

state ^{1}H CP/MAS Nuclear Magnetic Resonance respectively. More details about the

experimental characterization can be found in [23]. The elastic properties of the cell walls were

obtained from their main constituents found in literature [24] using an homogenisation law

divided into two consecutive rules of mixtures, following the procedure detailed in the appendix. As the lignin content is very low (less than 4% of the dry mass [17, 23]), the matrix was considered made of hemicellulose only for the calculations. Moreover, the Poisson's coefficient v_{TT}, which does not influence the tensile behaviour, was arbitrary set to 0.2 [25].

3.3. Boundary conditions

Boundary conditions were applied in order to simulate the experimental tensile testing conditions. The upper surface of the fibre was clamped (i.e. displacement at all nodes of the surface equal to 0 in all directions), and a displacement d was applied in the direction 3 to the nodes of the lower surface as represented in **Figure 4**, leading to the following equations, with U_1, U_2 and U_3 the displacements in the directions 1, 2 and 3 respectively:

Upper surface: $U_1 = U_2 = U_3 = 0$ *(6)*   Lower surface: $U_1 = U_2 = 0$; U_3 = d   *(7)*

The model is assumed linear elastic, therefore an arbitrary displacement corresponding to 1% deformation is applied and the global stress/strain curves are obtained by extrapolation in order to compare with experimental data. The study was conducted as a quasi-static simulation with a direct solver. The calculations were performed using a high-performance computer equipped with 1 TB of RAM and a bisocket architecture operating at 4.4 GHz.

The average stress and strain values are derived from the reaction forces and imposed displacement and thus calculated using the following equations, with F_3 the reaction force in the direction 3, S the surface of the filled fibre, d the displacement imposed and L the fibre length. The resulting stress is calculated from the mean between the surface integrals of the reaction forces at the nodes of both fibre edges since they have different surface areas.

$$\sigma = \frac{1}{2} \left(\frac{\iint F_{3\,(x=0)}}{S_{(x=0)}} + \frac{\iint F_{3\,(x=d)}}{S_{(x=d)}} \right) \qquad (8)$$

$$\varepsilon\,(\%) = 100 * \frac{d}{L} \qquad (9)$$

Following Hooke's law, Young's modulus is calculated as the ratio between the resulting engineering stress and strain values, and displayed for the different fibres employed in the study, as a function of their porosity content.

4. Results and discussion

4.1. Morphology of studied flax fibres

Volumetric quantification of fibre geometries and lumen was conducted on four fibres (a, b, c and d) by μ-CT. The variations of aspect ratio and cross-sectional surface areas along filled elements (excluding internal porosities) are evidenced in **Figure 5** and **Figure 6**, respectively. Mean fibre external transverse surface areas vary between 54 μm^2 and 192 μm^2 (**Table 2**). The aspect ratio is relatively constant along fibres **b, c**, with mean values between 1.04 and 1.26. However, fibre **a** is far from a circular idealization with a mean aspect ratio of 1.48. Variations along its length are highlighted by its higher standard deviation than fibres **b, c** (**Figure 6**). Finally, the fibre **d** presents an elliptical shape with a mean aspect ratio of 2.07. The porosity analysis shows that significant discrepancies are found between fibres (**Table 2**), with mean porosities reported between 0 and 7.2%. Moreover, the porosity content along fibres **a, b** and **c** varies greatly (**Figure 7**). Indeed, fibres **a** and **b** present porosity content close to zero at a few locations along their scanned length, indicating a narrowed lumen at some areas. These intricate shapes are further evidenced on the fibre longitudinal views and 3D views of the lumens (**Figure 7**). It should be noted that the lumen can possibly be under the detection limit allowed by the 150 nm voxel resolution at these particular areas. Interestingly, the lumen of fibre c is barely distinguishable along its length, apart from one particular location where it reaches almost 2%. This location, where a cavity adjacent to the lumen is observed, could be the consequence of a defect creation. Finally, no lumen was detectable for fibre d, perhaps as a consequence of a previous fibre deformation.

Few quantifications of the plant fibre porosity have been reported in literature, and even less on the impact on the mechanical properties. The values of porosities extracted from μ-CT data in this study, from 0 to 7.2% with a mean value of 2.5 ± 2.9% (**Table 2**), are in the same range as literature data for flax, depicting mean porosity content between 1.6 and 6.8% [17]. The inter-fibre and intra-fibre variability in terms of porosity were further highlighted in **Table 2** and **Figure 7**, leading to an intricate lumen shape, in agreement with work conducted on hemp by Beaugrand et al [12]. The precise description of the flax intricate shapes and hypothesis on the origin of these variabilities are further developed in a previous work conducted by the team [14]. The scenario includes variabilities originating from the location of observation along the fibres, different stages of the plant cell life, but also related to the processing stages involving drying [26-28], retting [29] and mechanical extraction from the stem possibly leading to lumen disruption and additional porosity close to defects [9, 10, 30, 31]. Additional experimental work would be required to better understand the contribution of the different mechanisms involved in the final shaping of the lumen. However, it is not the scope of the present work dedicated to investigate the consequences of these intricate fibre shapes on the mechanical properties.

4.2. Tensile performance of studied flax fibres

A mean Young's modulus of **39.3 ± 12.3 GPa**, strain at break of **2.24 ± 0.83** and strength of **700 ± 268 MPa** are reported. The important standard deviations reveal the dispersion of tensile behaviours widely reported for plant fibres. Compared to literature data on specimens tested with the same gauge length [32], the tensile properties appear in the average in terms of strain at break and in the lower bound in terms of Young's modulus and strength at break. Various sources of experimental and intrinsic variabilities have been widely described in literature [33, 34]. The differences observed might be explained by intrinsic physical parameters such as the fibre biochemical composition, diameter and ultrastructural parameters including the cellulose crystallinity and microfibril orientation as well as the defect content. Moreover, the strain

11

measurements are based on the cross-head displacements following the existing standard for tensile testing of plant fibres AFNOR NF T 25-501. Therefore, we can not exclude drawbacks from the method of measurement, and the use of an extensometer or DIC methods should be adapted to such small entities in the future for more accuracy. However, despite the high variability observed with tensile testing at the unitary fibre scale, we should mention that the properties are averaged in composites, where thousands of fibres are used. Therefore, Impregnated Fibre Bundle Tests (IFBT) appear as an interesting alternative taking into account the averaged back-calculated tensile properties and leading to lower scattering [17, 35, 36].

4.3. Overall predicted behaviour

The displacement applied in the tensile direction to the different fibres represented in **Figure 8**a validates the boundary conditions corresponding to a tensile test, i.e. clamping at the bottom and a maximal displacement around 1.4 μm corresponding to 1% deformation at the top. Moreover, the deformed fibres show an elongation in the direction 3 as well as a shrinkage in the directions 1 and 2 compared to the initial structures (dark outlines). The displacements in the directions 1 and 2 in **Figure 9** reveal asymmetrical displacement field induced by the geometry (orientation and sectional variation) of the fibres. The assumed linear-elasticity allows to capture the stress heterogeneity at the surface of the fibres from X-ray μ-CT, as illustrated by the stress component $\sigma 33$ (**Figure 8**b). The examination of this component reveals stress heterogeneity according to the loading condition and fibre morphology. Since the fibre has a yield stress, the continuous increase in loading magnitude does not allow to capture the real stress component magnitude which is for its high level overestimated in the present model. However, the model still captures the stress concentrations induced by the surface roughness. To the contrary, the cylindrical model fibre exhibits homogeneous values.

Figure 10 depicts the estimated Young's modulus as a function of porosity for all studied fibres. For the model fibre, a perfectly linear relationship between Young's modulus and porosity content (p) is observed, with a decrease of 10% for a porosity content of 10% compared to the filled fibre:

$$E \; (GPa) = -0.651 * p(\%) + 65{,}07; \; R^2 = 1 \qquad (10)$$

Therefore, it follows a rule of mixtures when considering the fibre as a two-phases composite made of cell material and air. In fact, several models have been developed in order to assess the relationship between Young's modulus and porosity content for various materials [37]. In the case of low porosity content (generally less than 10%), the reduction of Young's modulus is only influenced by the void fraction and the relationship is linear since the main deformation mechanism is tensile loading, i.e. no flexion is induced by the void structure. The diameter dependency of Young's modulus was also investigate by Placet et al. [24] with an analytical model based on the thick laminated composite tube model. Contrary to our study, the authors considered the fibre cross-section with lumen instead of the filled cross-section for the calculations and observed a trend in the same range: an underestimation between 15 and 25% of Young's modulus for a lumen content varying between 10 and 20%. Although the influence on Young's modulus of such low porosity content (inferior to 7%, as depicted by μ-CT) is minor, the damage mechanisms might be more impacted.

A similar linear relationship can be found for the fibres a, b, c, d with no variation along the length of the fibres (Fibres-NV):

$$E \; (GPa) = -0.706 * p(\%) + 65.08; \; R^2 = 1 \qquad (11)$$

Consequently, the fibre morphology does not seem to influence the overall Young's modulus in this model under the assumption of linear elasticity and MFA=0°. This is contradictory to the

findings of Gassan et al. [18] or Del Masto et al. [19], who concluded to the influence of the degree of ellipticity on Young's modulus. In particular, Del Masto et al. highlighted a decrease in apparent stiffness of hemp fibres with increasing degree of ellipticity due to the introduction of heterogeneous axial and shear stresses and strains in the cell walls. However, they have shown that the origin of this behaviour is not purely geometrical but enhanced by different factors such as the microfibril initial orientation and reorientation upon tensile testing, or viscoelasticity, which are not considered in this model.

For fibres a, b, c, d with variation along their length, the slope is steeper, i.e. Young's modulus decreases more drastically with the porosity content, i.e. a 5% porosity content lead to more than 12% decrease for Young's modulus, and the determination coefficient is lower ($R^2 = 0.92$). In order to better understand the origin of the differences observed for the fibres a, b, c and d, the evolution of the position of the centres of mass along the cross-sections of fibres a, b, c and d are plotted in **Figure 11**. The centres of mass are calculated as the brightness-weighted average of the x and y coordinates of all pixels. It reveals that the centre of mass of each fibre varies between 0.5 and 1.5 μm along both directions, which is far from being negligible for fibres with diameters between 10 to 20 μm. Moreover, the highest variations are observed for fibres a and d. The possible origin of theses variations along the fibre length are further illustrated in **Figure 11b**, where the evolution of centre of mass along a typical fibre presenting an irregular shape and not perfect alignment with respect to the tensile direction is schematically represented. By comparing Young's moduli of the filled fibres with and without variations along their length (**Figure 12**), it can be seen that the filled fibres without variations along their length (-F-NV) exhibit the same Young's modulus around 65 GPa. Consequently, different fibre cross-sectional shapes kept constant along the fibres do not influence the stiffness in such simple model (elastic domain, MFA=0). On the other hand, strong differences are observed for the corresponding fibres with variations along their length (-F). In particular, Young's modulus of the fibres a and

d decrease of respectively 11% and 2%, whereas the difference is negligible for fibres b and c. As a result, **the deviation from the rule of mixtures could be attributed at least partly to the variations of the position of the centres of mass along the fibres**, and especially for fibres a and d which exhibits the highest modulus and centre of mass deviations as highlighted in **Figure 11,** explaining their lower values when taking into account the lumen in **Figure 10**. Therefore, although the mode of solicitation is purely uniaxial, the stress transfer is not fully in tension: shearing is induced by geometrical considerations. Consequently, the modulus calculated from the reaction forces in the tensile direction cannot be considered as the longitudinal modulus, but it is more the result of the presence of a combination of longitudinal and shear stresses. Several origins for the variation in the position of the centre of mass are suggested: variabilities of surface areas usually observed along plant fibres [3, 38], but also twist [39, 40] and not perfect alignment [41] during X-ray μ-CT experiments. Both contributions cannot be solely separated but they reflect the intrinsic and experimental variabilities encountered with plant fibres.

4.4. Predicted stress heterogeneity

The resulting axial and shear stress distributions along fibres a, b, c, d and M-3 are plotted on longitudinal cross-sections in the (13) and (23) planes in **Figure 13** and **Figure 14** respectively**.** The mean values of axial stresses σ_{33} in the tensile direction on the overall volume are quite similar for all fibres. However, the distribution of σ_{33} shows heterogeneities both at the surface and within the cell walls at a different extend for fibre a, b, c and d (**Figure 13a**). The stress distributions of σ_{11} and σ_{22} also highlight stress concentrations (**Figure 13b** and **c**). However, the mean stress levels are negligible compared to σ_{33} and will not be addressed in the rest of the study. No shear stresses implicating the tensile direction σ_{13} and σ_{23} are discernible on the model fibre apart from close to the boundaries (**Figure 14a** and **b**). However, both shear stress

inhomogeneities seem enhanced by the presence of surface roughness, variations of external outlines and lumen shapes along the fibres a, b, c, d. The values range from negative to positive similarly for σ_{13} and σ_{23}. In addition, the shear stresses σ_{12} not involving the tensile direction are marginal (**Figure 14c**) and will not be addressed in the rest of the study.

The stress concentrations of the most contributing stress components in tensile testing (i.e. σ_{33}, σ_{13} and σ_{23}) were further quantified by plotting their maximum values on transverse cross-sections 5 µm apart along the fibres (plane 12), as well as resulting stress fields at particular locations of interest (**Figure 15** and **Figure 16**). Therefore, high axial stress concentrations are observed along the fibres a, b, c, d (**Figure 15**), reaching 4500 MPa for fibre c at a particular location. Even if the values are unrealistic due to the assumption of linear elasticity, it highlights the possible stress concentration induced by both surface roughness and intricate lumen shape, as evidenced by the profiles 1 and 2 plotted along the diameter of fibre c (**Figure 15**-bottom). In comparison, their related fibres without variation along their length (NV) show almost constant maximum axial stress between 750 and 850 MPa when excluding the stress concentrations induced by the boundary conditions at the edges.

The maximum shear stresses σ_{13} and σ_{23} involving the direction of tensile loading are plotted in **Figure 16**. As for axial stress, the variation along the fibres seems to enhance the heterogeneity of the shear stress field, with maximum shear stresses between 50 and 250 MPa whereas they do not reach more than 35 MPa for the fibres -NV and M-0. Therefore, it confirms the presence of shear stress concentrations within the fibre cell walls when taking into account the morphology variations along the fibres a, b, c and d (**Figure 11**). In literature, few models considered variations of sections along the fibres. In particular, a sinusoidal variation of cross-section along circular and elliptical fibres was used in the FEA developed by Del Masto et al.[42], showing no consequence on the tensile response in terms of shape but high stress concentrations induced by the varying cross-sections. In our study which considers a more

complex fibre external shape and internal lumen than previous studies, the results of the numerical model confirmed that both lumen intricate shape and surface roughness are sites of stress concentrations. The axial stress concentrations as can be seen close to the internal porosities of the fibres from tomography in **Figure 13** or on the enlarged area of fibre c and related line plots in **Figure 15 (**bottom**)** are induced by geometrical singularities, and more precisely the curvatures in the direction perpendicular to the tensile loading. Finally, heterogeneous shear stresses involving the tensile direction are also introduced by the geometrical considerations (i.e. variations of cross-sections and misalignment with respect to the tensile direction) as evidenced in **Figure 14** and **Figure 16.** It could therefore contribute to the decrease of Young's modulus observed in **Figure 10** compared to the values predicted by a rule of mixtures. Moreover, shear stress might also be involved in the initiation or propagation of fibre failure. In conclusion, both surface roughness, lumen intricate shape or even smaller cavities characterizing defected areas could therefore be in competition to drive the failure of the fibre by different loading paths (i.e. shear or tensile), depending on which will require less energy to propagate the crack at the crack tip following Griffith's criteria [43]. Consequently, the damage analysis by *in situ* surface observation such as optical or electronic microscopy under mechanical loading does not appear as a reliable method to detect bulk rupture mechanisms. In particular, complementary work should be conducted in the future by taking into account defects and performing *in situ* tensile testing and high-resolution X-ray μ-CT, allowing to decipher the various mechanisms leading to the fibre failure.

As a result, the stress-strain curves of fibres a, b, c and d and the extreme model fibres with porosity content of 0 and 10% (M-0 and M-10) are displayed in **Figure 17**, together with the experimental data for the Bolchoï variety. Therefore, differences of porosity content and geometrical considerations inducing shearing despite a tensile loading seem to partly explain the scattering of behaviours observed experimentally. However, Young's moduli are

overestimated compared to experimental data, and the non-linearities are not taken into account by the rather strong hypothesis of the model, i.e. linear elasticity and microfibril angle equal to 0.

5. Conclusions

The consequences of the flax intricate morphology on its tensile properties were investigated by implementing a finite element model in the elastic domain based on tomography volumes. Axial and shear stress concentrations were observed close to the intricate lumen shape and surface roughness, highlighting their potential to act as crack departure depending on their geometry. In particular, maximum axial stresses between 1000 and 4500 MPa and maximum shear stresses between 50 and 250 MPa were reported along the fibres from μ-CT, indicating stress concentrations even if the values are not realistic due to the linear elastic assumption. Moreover, Young's modulus was shown to decrease with the increase of porosity content more drastically than a simple rule of mixtures, attributed to the shear induced by geometrical considerations. Indeed, both the intrinsic variability of diameter along the fibres and not perfect alignment of the fibre with respect to the tensile direction influence the resulting tensile stiffness. As a prospect, the microfibril orientation and reorientation upon tensile testing will be studied experimentally and integrated in the model in order to better fit the experimental data. A further step would be to take into account other phenomena such as viscous and plastic behaviours, as well as to investigate other types of mechanical solicitations and environments that reflect the variety of conditions being encountered during a composite part lifetime.

References

[1] Partanen A, Carus M. Biokomposite: überzeugende Lösungen aus erneuerbaren Materialien. Nova-Institute. 2020.

[2] Le Duigou A, Davies P, Baley C. Environmental Impact Analysis of the Production of Flax Fibres to be Used as Composite Material Reinforcement. Journal of Biobased Materials and Bioenergy. 2011;5(1):153-65.

[3] Charlet K, Jernot J-P, Breard J, Gomina M. Scattering of morphological and mechanical properties of flax fibres. Industrial Crops and Products. 2010;32(3):220-4.

[4] Coroller G, Lefeuvre A, Le Duigou A, Bourmaud A, Ausias G, Gaudry T, et al. Effect of flax fibres individualisation on tensile failure of flax/epoxy unidirectional composite. Composites Part A: Applied Science and Manufacturing. 2013;51:62-70.

[5] Mattrand C, Béakou A, Charlet K. Numerical modeling of the flax fiber morphology variability. Composites Part A: Applied Science and Manufacturing. 2014;63:10-20.

[6] Charlet K, Jernot JP, Eve S, Gomina M, Bréard J. Multi-scale morphological characterisation of flax: From the stem to the fibrils. Carbohydrate Polymers. 2010;82(1):54-61.

[7] Madsen B, Gamstedt EK. Wood versus Plant Fibers: Similarities and Differences in Composite Applications. Advances in Materials Science and Engineering. 2013:1-14.

[8] Thuault A. Approche multi-échelle de la structure et du comportement mécanique de la fibre de lin, PhD thesis: Caen; 2011.

[9] Hernandez-Estrada A, Reza M, Hughes M. The Structure of Dislocations in Hemp (Cannabis sativa L.) Fibres and Implications for Mechanical Behaviour. BioResources. 2020;15:2579-95.

[10] Zhang H, Sui T, Thygesen LG, O'brien P, Korsunsky A. Multi-modal Microscopy Characterisation of Nodal Markings in Flax Fibre. World Congress on Engineering London2015.

[11] Aslan M, Chinga-Carrasco G, Sørensen BF, Madsen B. Strength variability of single flax fibres. Journal of Materials Science. 2011;46(19):6344-54.

[12] Beaugrand J, Guessasma S, Maigret JE. Damage mechanisms in defected natural fibers. Scientific Reports. 2017;7(1):14041.

[13] Abbey B, Eve S, Thuault A, Charlet K, Korsunsky A. Synchrotron X-Ray Tomographic Investigation of Internal Structure of Individual Flax Fibres. In: Proceedings I, editor. 6th World Congress of Biomechanics (WCB 2010). Singapore2010. p. 1151-4.

[14] Richely E, Durand S, Melelli A, Kao A, Magueresse A, Dhakal H, et al. Novel Insight into the Intricate Shape of Flax Fibre Lumen. Fibers. 2021;9(4).

[15] Baley C, Perrot Y, Busnel F, Guezenoc H, Davies P. Transverse tensile behaviour of unidirectional plies reinforced with flax fibres. Materials Letters. 2006;60(24):2984-7.

[16] Ahmed S, Ulven C. Dynamic In-Situ Observation on the Failure Mechanism of Flax Fiber through Scanning Electron Microscopy. Fibers. 2018;6(1).

[17] Richely E, Bourmaud A, Placet V, Guessasma S, Beaugrand J. A critical review of the ultrastructure, mechanics and modelling of flax fibres and their defects. Progress in Materials Science. 2021;124(100851):1-31.

[18] Gassan J, Chate A, Bledzki AK. Calculation of elastic properties of natural fibers. Journal of Materials Science. 2001;36:3715-20.

[19] Del Masto A, Trivaudey F, Guicheret-Retel V, Placet V, Boubakar L. Nonlinear tensile behaviour of elementary hemp fibres: a numerical investigation of the relationships between 3D geometry and tensile behaviour. Journal of Materials Science. 2017;52:6591-610.

[20] Legland D, Arganda-Carreras I, Andrey P. MorphoLibJ: integrated library and plugins for mathematical morphology with ImageJ. Bioinformatics. 2016;32(22):3532–4.

[21] Rihouey C, Paynel F, Gorshkova T, Morvan C. Flax fibers: assessing the non-cellulosic polysaccharides and an approach to supramolecular design of the cell wall. Cellulose. 2017;24(5):1985-2001.

[22] Melelli A, Jamme F, Legland D, Beaugrand J, Bourmaud A. Microfibril angle of elementary flax fibres investigated with polarised second harmonic generation microscopy. Industrial Crops and Products. 2020;156(112847):1-10.

[23] Richely E. Combined experimental end numerical approaches to understand the structure-mechanical property relashionship of flax fibres and bundles, PhD thesis. Nantes, France: University of Nantes; 2021.

[24] Placet V, Trivaudey F, Cisse O, Gucheret-Retel V, Boubakar ML. Diameter dependence of the apparent tensile modulus of hemp fibres: A morphological, structural or ultrastructural effect? Composites Part A: Applied Science and Manufacturing. 2012;43(2):275-87.

[25] Del Masto A, Trivaudey F, Guicheret-Retel V, Placet V, Boubakar L. Nonlinear tensile behaviour of elementary hemp fibres: a numerical investigation of the relationships between 3D geometry and tensile behaviour. Journal of Materials Science. 2017(52):6591–610.

[26] Morvan C, Andème-Onzighi C, Girault R, Himmelsbach DS, Driouich A, Akin DE. Building flax fibres: more than one brick in the walls. Plant Physiology and Biochemistry 2003;41:935-44.

[27] Milthorpe FL. Fibre Development of Flax in Relation to Water Supply and Light Intensity. Annals of Botany. 1945;IX(33):31-53.

[28] Gibaud M, Bourmaud A, Baley C. Understanding the lodging stability of green flax stems; The importance of morphology and fibre stiffness. Biosystems Engineering. 2015;137:9-21.

[29] Akin DE. Linen most useful: perspectives on structure, chemistry, and enzymes for retting flax. ISRN Biotechnol. 2013:186534.

[30] Wang HM, Wang X. Surface morphologies and internal fine structures of bast fibers. Fibers and polymers. 2005;6(1):6-12.

[31] Rask M, Madsen B, Sørensen BF, Fife JL, Martyniuk K, Lauridsen EM. In situ observations of microscale damage evolution in unidirectional natural fibre

composites. Composites Part A: Applied Science and Manufacturing. 2012;43(10):1639-49.

[32] Baley C, Bourmaud A. Average tensile properties of French elementary flax fibers. Materials Letters. 2014;122:159-61.

[33] Feigel B, Robles H, Nelson JW, Whaley JMS, Bright LJ. Assessment of Mechanical Property Variation of As-Processed Bast Fibers. Sustainability. 2019;11(9).

[34] Bourmaud A, Beaugrand J, Shah DU, Placet V, Baley C. Towards the design of high-performance plant fibre composites. Progress in Materials Science. 2018;97:347-408.

[35] Bensadoun F, Verpoest I, Baets J, Müssig J, Graupner N, Davies P, et al. Impregnated fibre bundle test for natural fibres used in composites. Journal of Reinforced Plastics and Composites. 2017;36(13):942-57.

[36] Shah DU, Nag RK, Clifford MJ. Why do we observe significant differences between measured and 'back-calculated' properties of natural fibres? Cellulose. 2016;23(3):1481-90.

[37] Morrissey LS, Nakhla S. A Finite Element Model to Predict the Effect of Porosity on Elastic Modulus in Low-Porosity Materials. Metallurgical and Materials Transactions A. 2018;49(7):2622-30.

[38] Thomason JL, Carruthers J, Kelly J, Johnson G. Fibre cross-section determination and variability in sisal and flax and its effects on fibre performance characterisation. Composites Science and Technology. 2011;71(7):1008-15.

[39] Placet V, Cissé O, Lamine Boubakar M. Nonlinear tensile behaviour of elementary hemp fibres. Part I: Investigation of the possible origins using repeated progressive

loading with in situ microscopic observations. Composites Part A: Applied Science and Manufacturing. 2014;56:319-27.

[40] Page DH, El-Hosseiny F, Winkler K. Behaviour of single wood fibres under axial tensile strain. Nature. 1971;229:252-3.

[41] Islam F, Joannès S, Laiarinandrasana L. Evaluation of Critical Parameters in Tensile Strength Measurement of Single Fibres. Journal of Composites Science. 2019;3(3).

[42] Del Masto A. Transition d'échelle entre fibre végétale et composite UD : propagation de la variabilité et des non-linéarités, PhD thesis: Bourgogne Franche-Comte; 2018.

[43] Griffith AA. The phenomena of rupture and flow in solids Philosophical Transactions od the Royal Society of London Series A, Containing Papers of a Mathematical of Physical Character. 1921;221:163-98.

Figure captions

Figure 1: General approach of FEA based on 3D geometries obtained by X-ray μ-CT.

Figure 2: Meshings of different coarseness, resulting axial stress component σ_{33} (in Pa) and Young's modulus (GPa) as a function of the degrees of freedom.

Figure 3: (a) Young's modulus as a function of the filled model fibre length, (b) Maximum axial stress σ_{33} along the filled model fibre of 140 μm.

Figure 4: Transverse isotropic model with MFA=0: inputs.

Figure 5: Evolution of the external transverse surface area along four flax fibres (a, b, c and d), from X-ray microtomography data.

Figure 6: Evolution of the aspect ratio along four flax fibres (a, b, c and d), from X-ray microtomography data.

Figure 7: Porosity profile along four flax fibres (a, b, c and d), corresponding longitudinal cross-sections of the fibres and 3D views revealing the internal lumen after image processing (right).

Figure 8: (a) Displacement in the tensile direction 3 corresponding to 1% deformation applied to the fibres, with initial fibre geometries in black; (b) resulting axial stress component σ_{33}, in the plane (23).

Figure 9: Top: Displacement in the direction 1 corresponding to 1% deformation applied to the fibres in the plane (13); bottom: Displacement in the direction 2 corresponding to 1% deformation applied to the fibres in the plane (23).

Figure 10: Numerically predicted Young's modulus of the different fibres used in the study as a function of their porosity content, and related linear fit.

Figure 11: (a) Evolution of the position of the centres of mass along the cross-sections of fibres a, b, c and d; (b) Example of mass centre evolution along a fibre with irregular shape and misalignment with respect to the fibre axis.

Figure 12: Young's modulus of filled fibres from X-ray microtomography with (-F) and without variations along their length (-NV-F).

Figure 13: Distribution of axial stresses (a) σ_{33}, (b) σ_{11} and (c) σ_{22} on longitudinal cross-sections of different fibres in the planes (13) and (23).

Figure 14: Distribution of shear stresses (a) σ_{13}, (b) σ_{23} and (c) σ_{12} on longitudinal cross-sections of different fibres in the planes (13) or (23).

Figure 15: Top: Maximum axial stress σ_{33} along cross-sections of fibres a, b, c and d with and without variations along their length as well as model fibre M-0; bottom: axial stress along a longitudinal cross-section of fibre c with and without variation along its length, and resulting axial stress profile along two lines (1 and 2).

Figure 16: Maximum shear stresses σ_{13} and σ_{23} along cross-sections of fibres a, b, c and d with and without variations along their length, and model fibre M-0.

Figure 17: Experimental stress-strain curves and resulting from the FEA of fibres a, b, c, d and the model fibre with porosity content of 0 and 10% (M-0 and M-10).
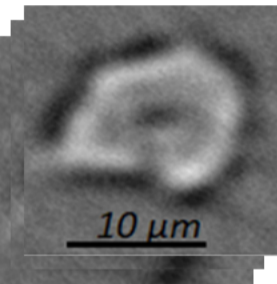
| Grey-scale cross-sections | Binarized 3D volume, *Fiji* | Meshed 3D volume, *Simpleware ScanIP* | FEA, *Comsol Multiphysics ® v5.4* |
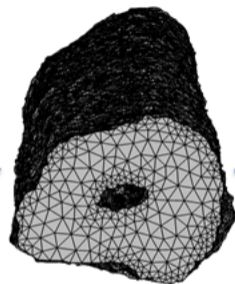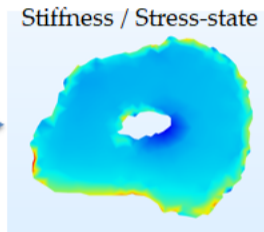
Stiffness / Stress-state

10 µm
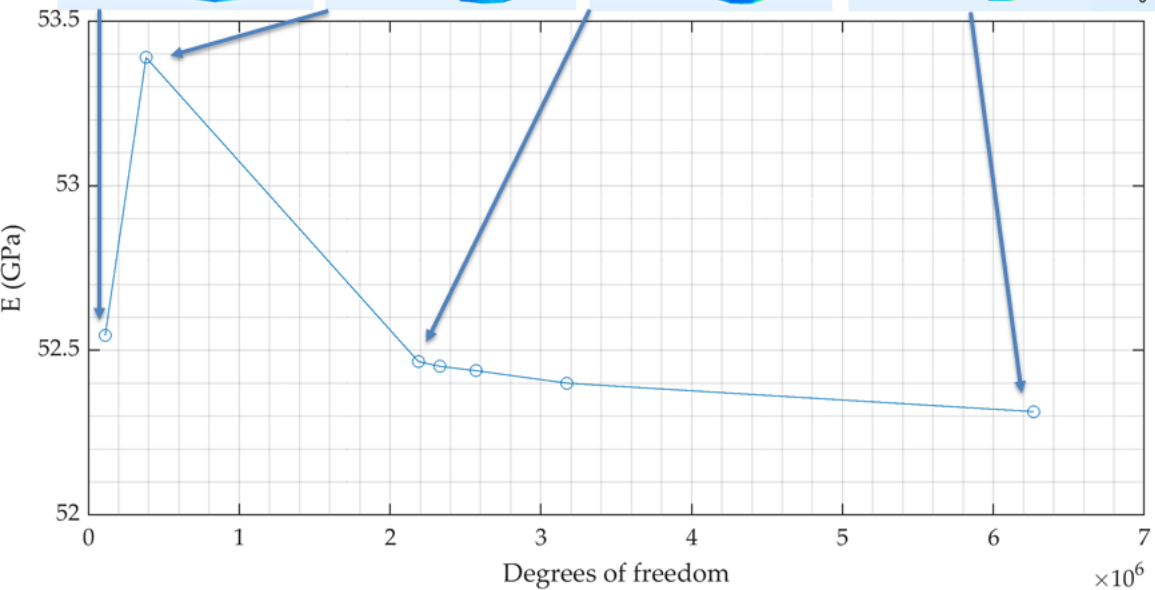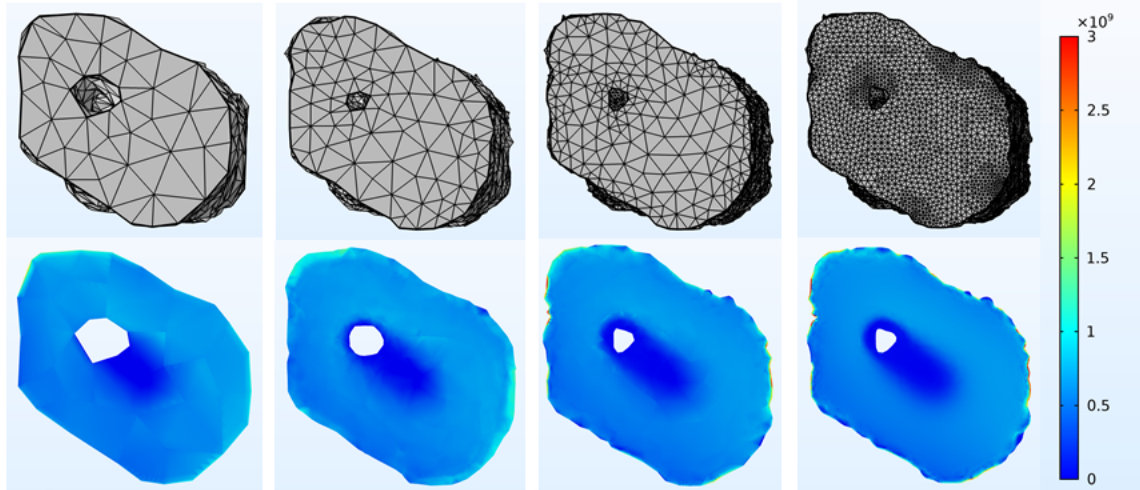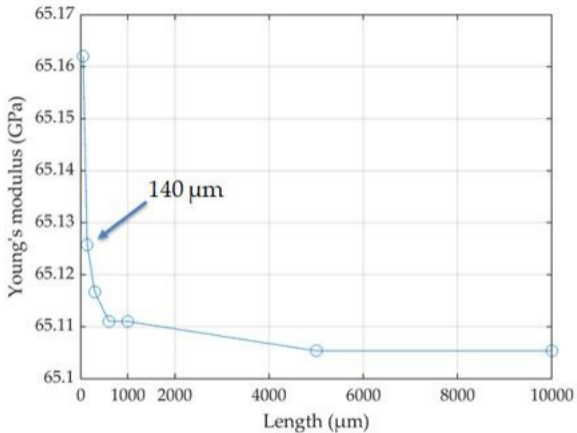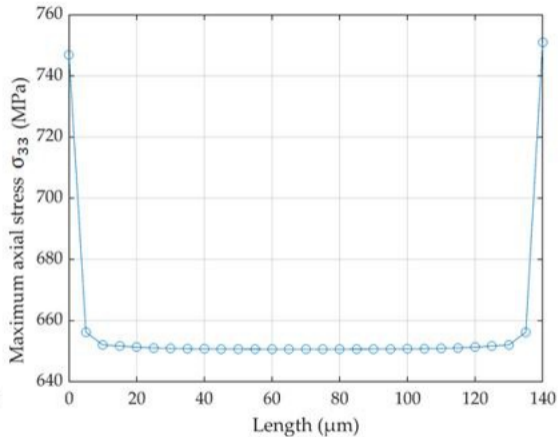
(a)   (b)

% of components	
$\%m_{cellulose}$	75
Cristallinity rate	0.6
$\%m_{hemicell}$	100
$\%m_{lignine}$	0

Biochemical analysis
Nuclear Magnetic Resonance

Properties of components

From literature data

Elastic properties	
E_L	65 GPa
E_T	9.8 GPa
G_{LT}	3.2 GPa
G_{TT}	4.1 GPa
ν_{LT}	0.18
ν_{TT}	0.2

Homogenisation law

Estimation for flax (MFA = 0°)

Displacement d

Clamping
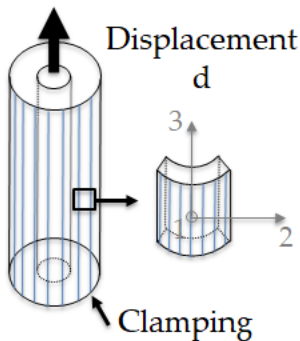
Long fibre reinforced composite material

Elements type and formulation:
Tetrahedrons (5.10^5 to 5.10^6 dof)
Quadratic discretization

Fibre a

Fibre b

Lumen from fibre a

Lumen from fibre b

Lumen from fibre c

Fibre c

Fibre d

Figure showing Young's modulus (GPa) versus Porosity (%). Legend: Fibres (○), Model (×), Fibres - NV (✱). Data points labeled a, b, c, d. Model line with $R^2 = 1$, Fibres - NV line with $R^2 = 1$, and Fibres line with $R^2 = 0.919$.

(a) (b)

(a)

M-3 a b c d σ_{33}

N/m^2
x10^9

(b)

M-3 a b c d σ_{11}

N/m^2
x10^8

(c)

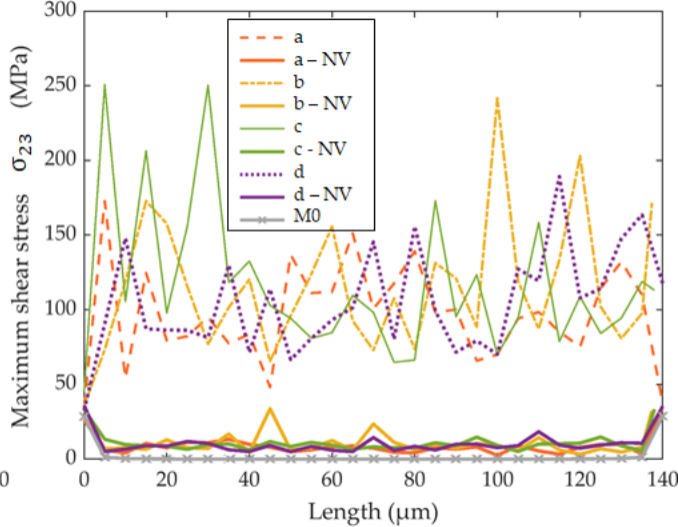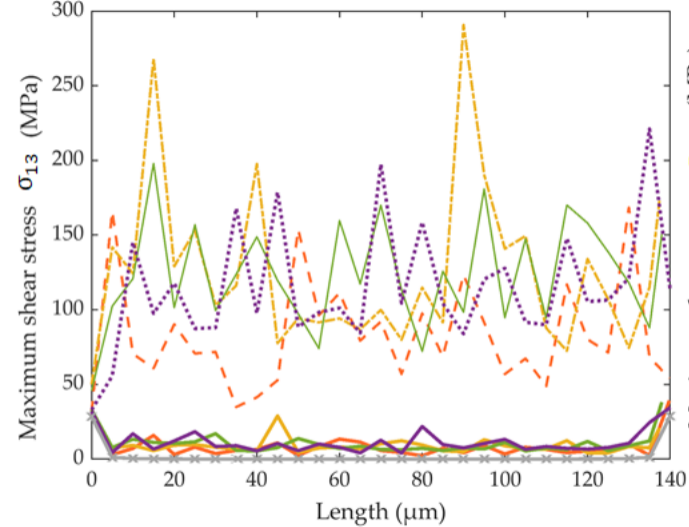M-3 a b c d σ_{22}
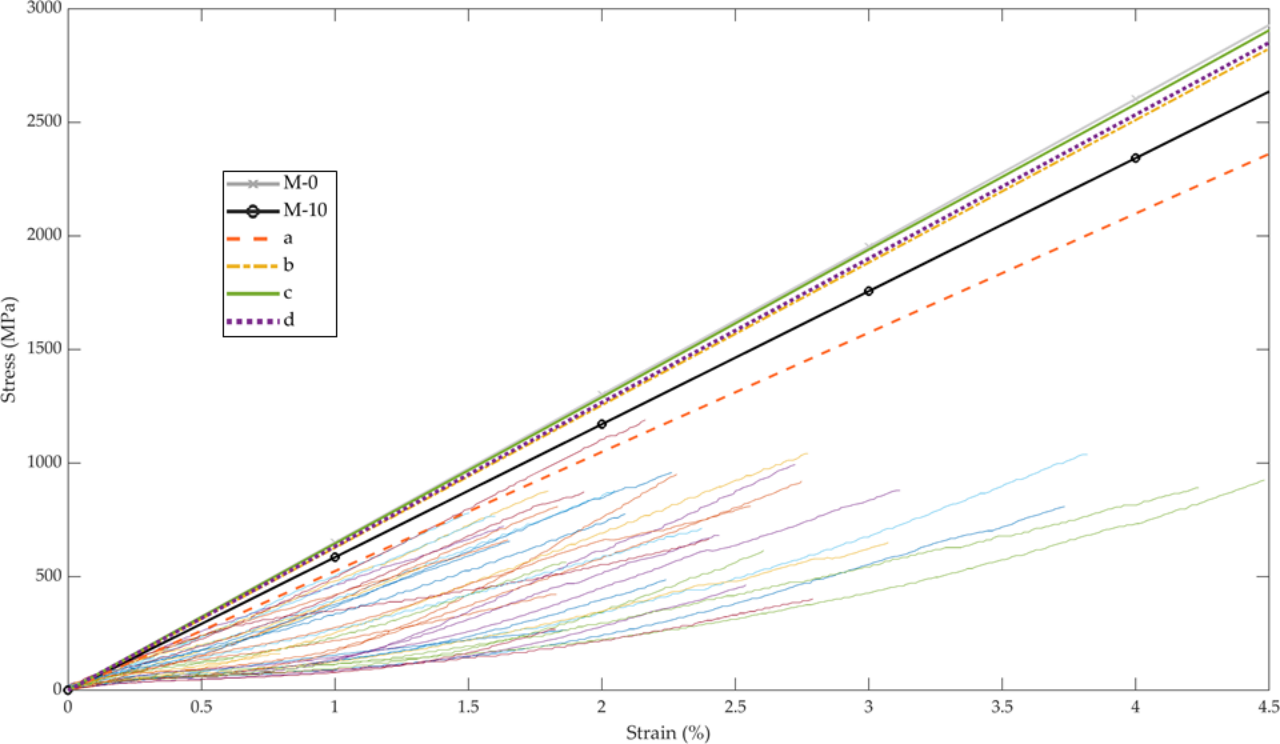
N/m^2
x10^8
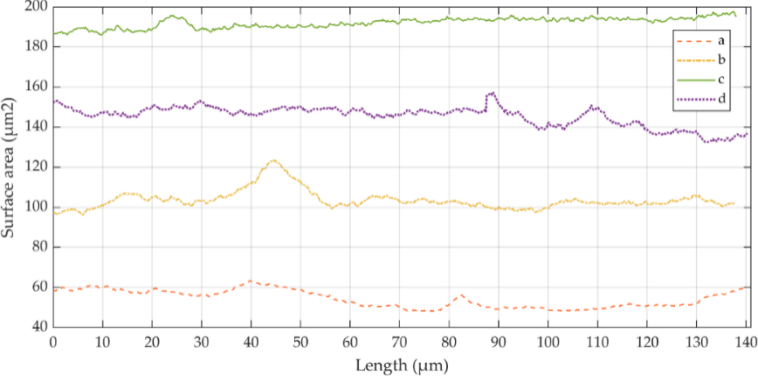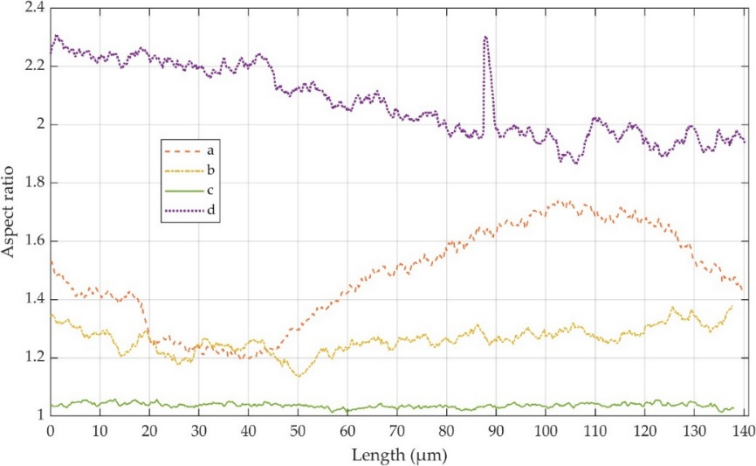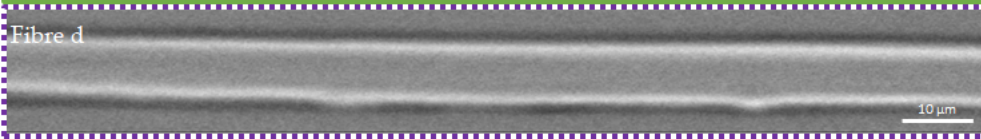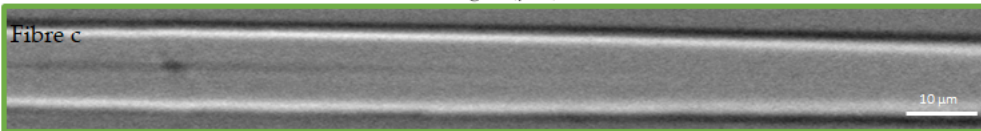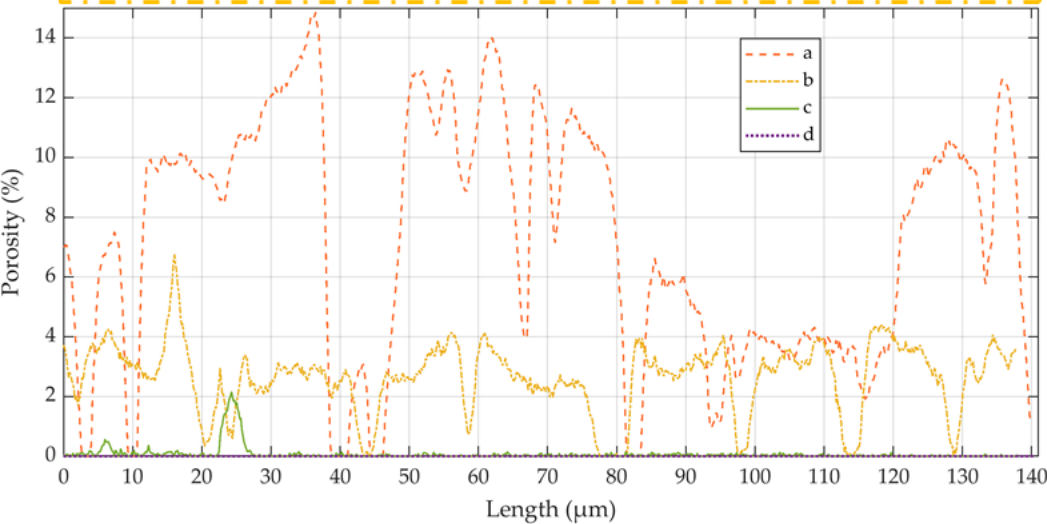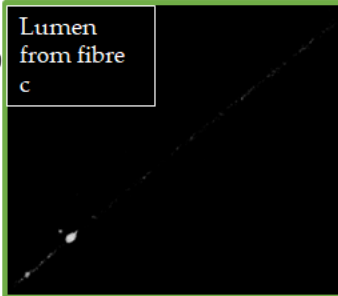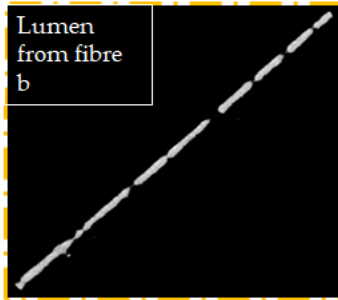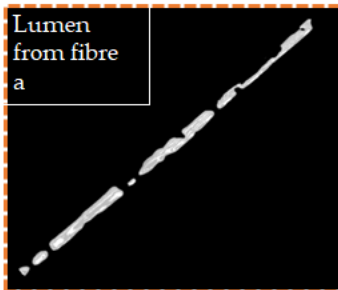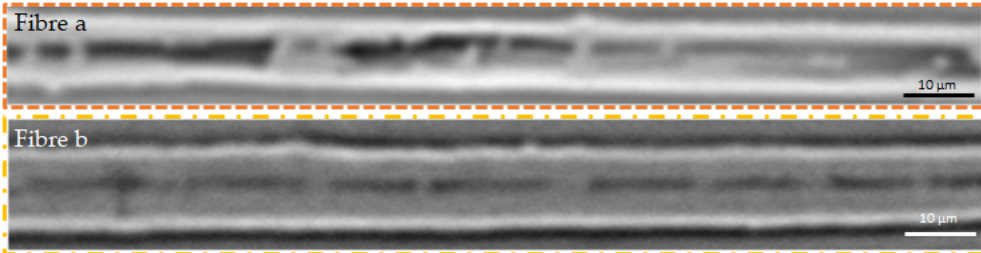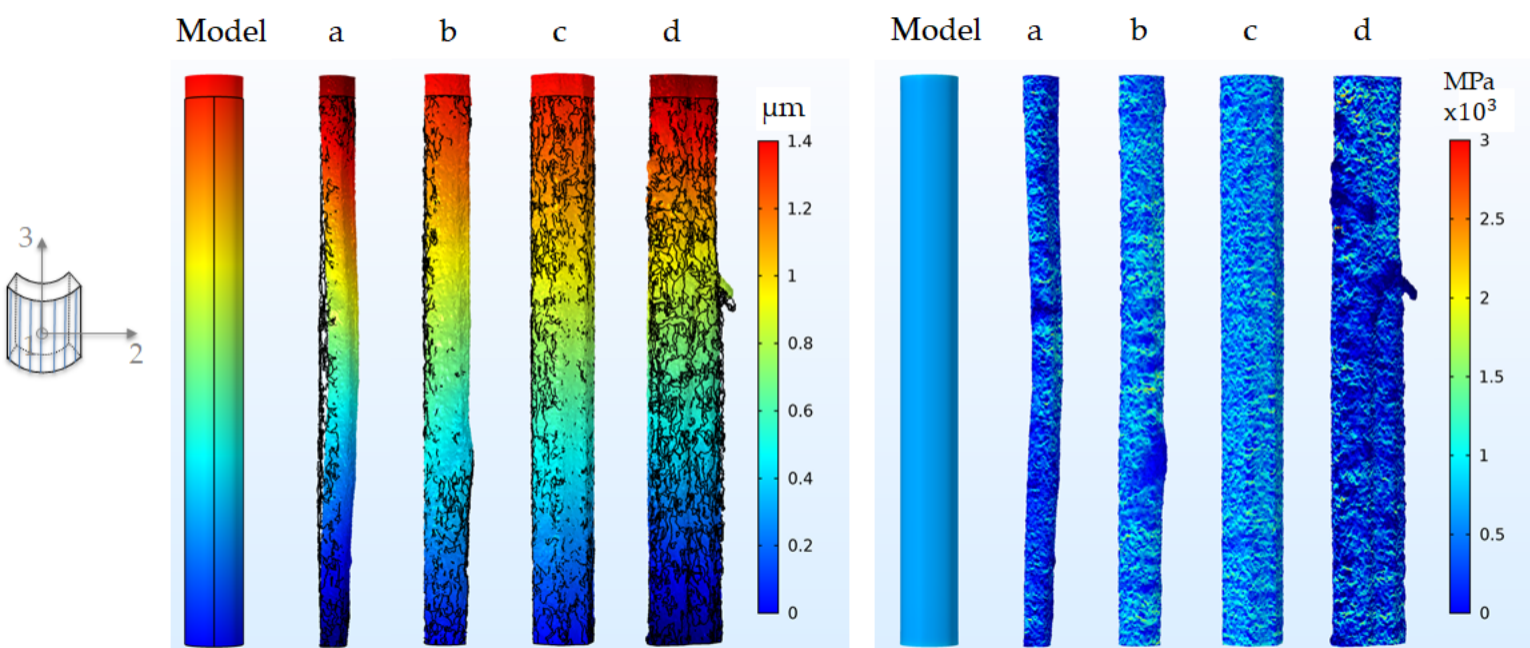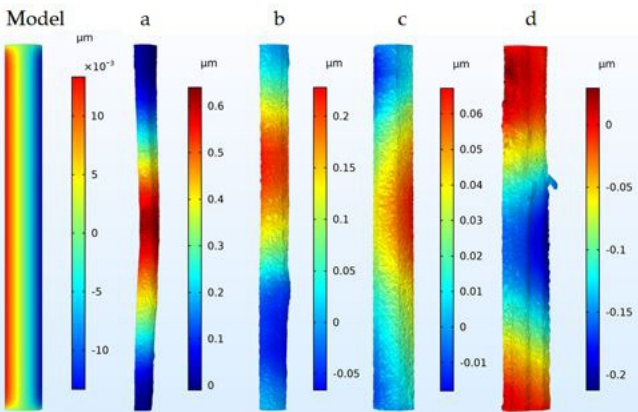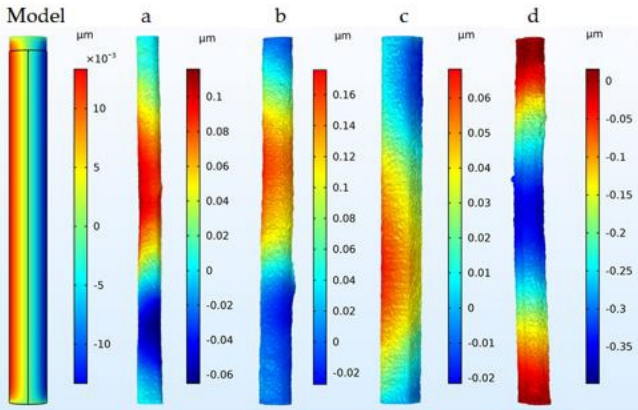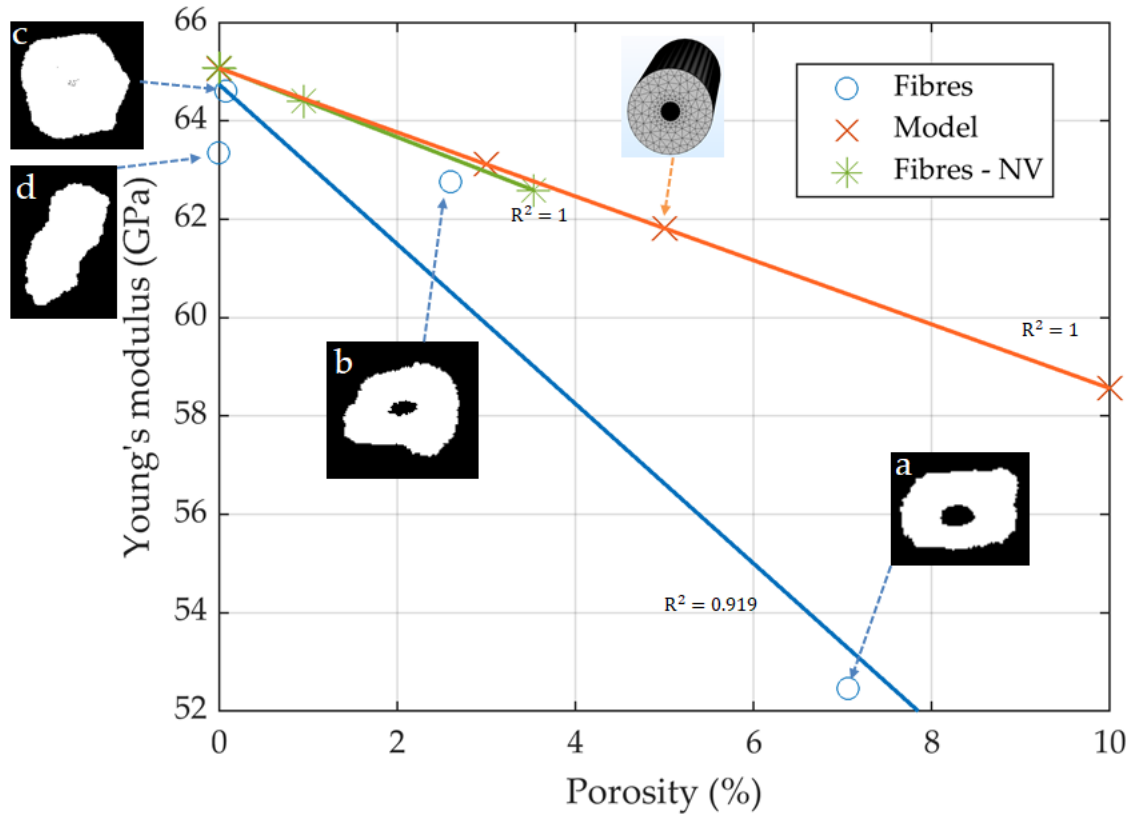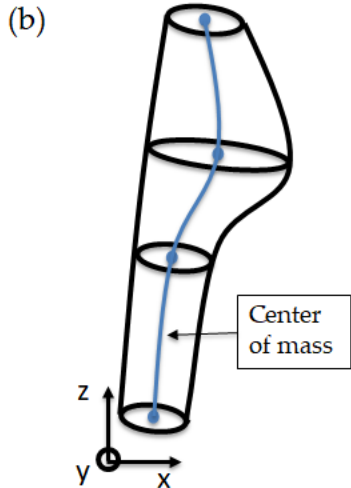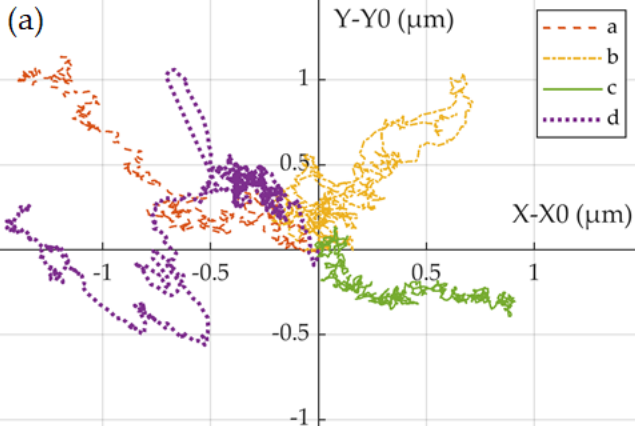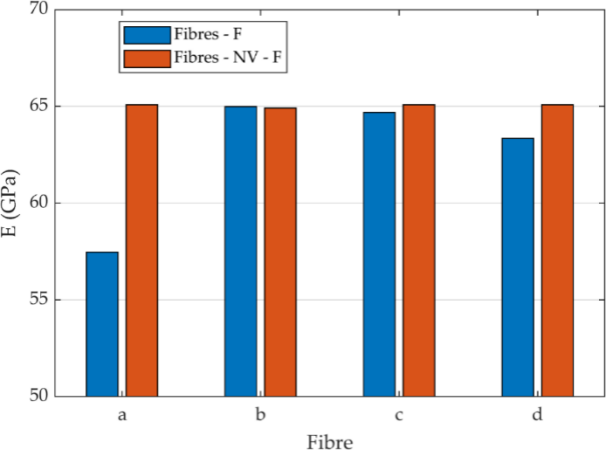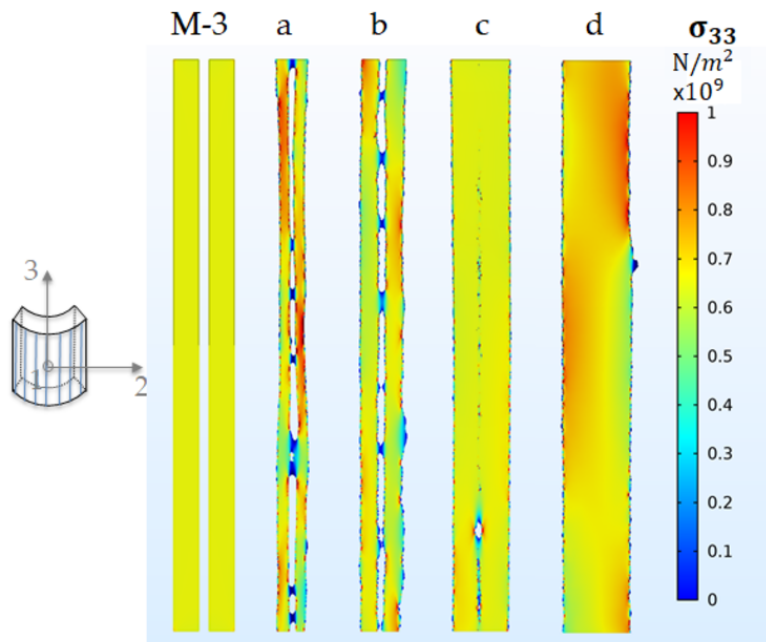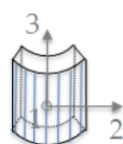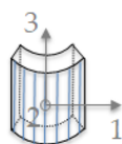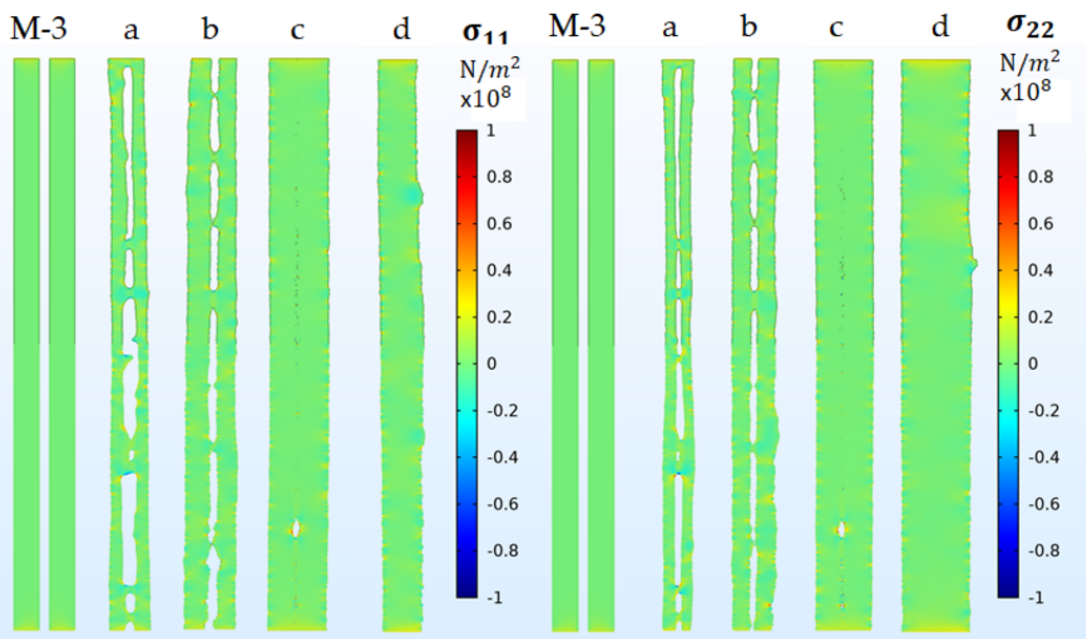
(a)

(b)
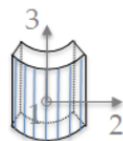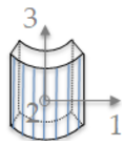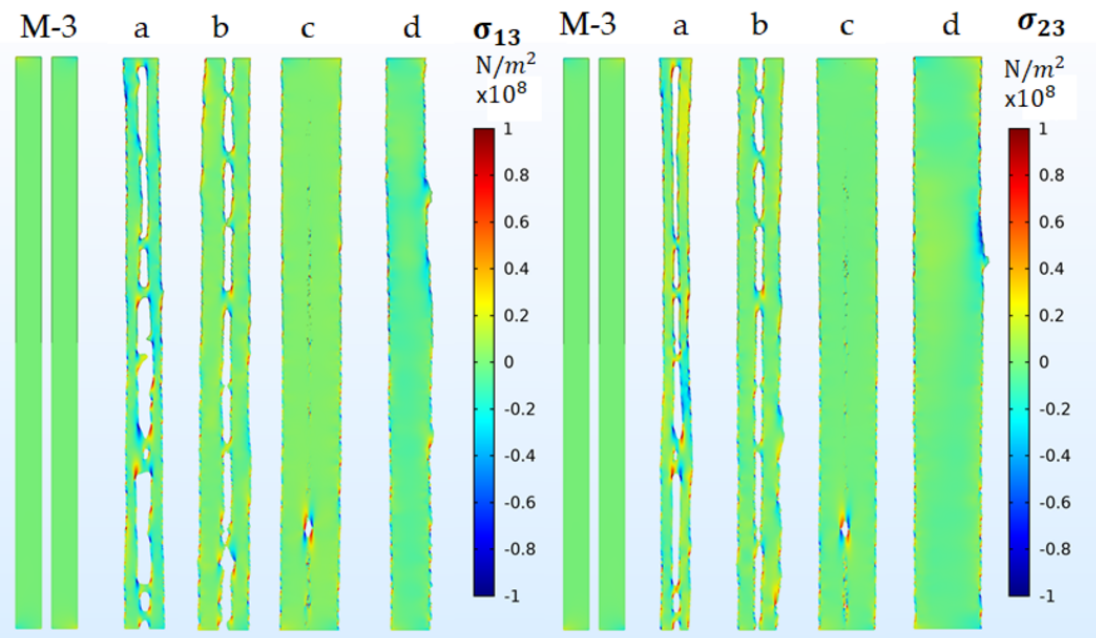
(c)
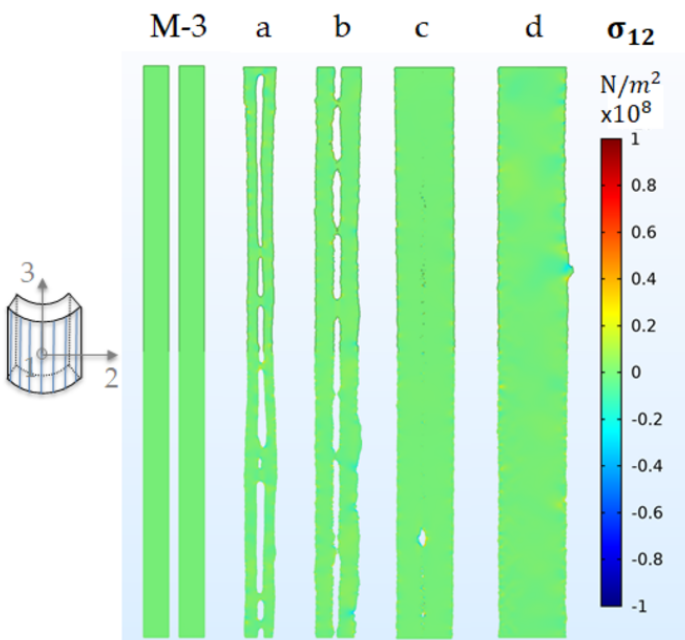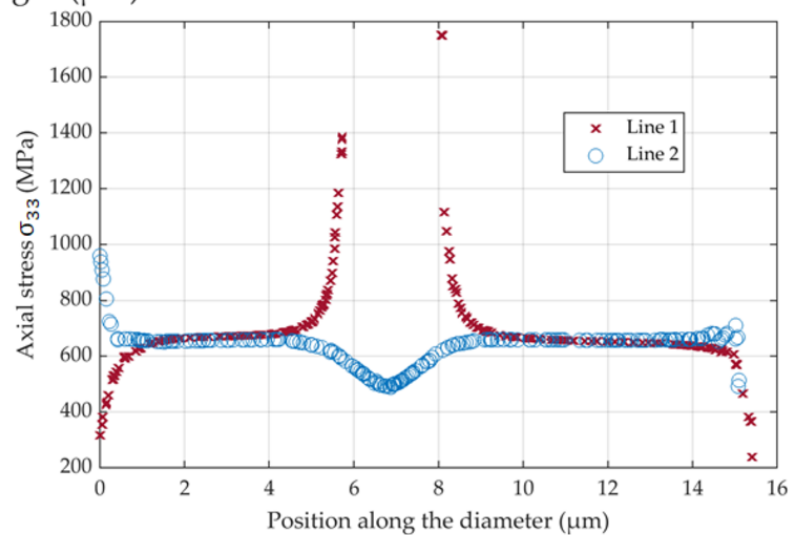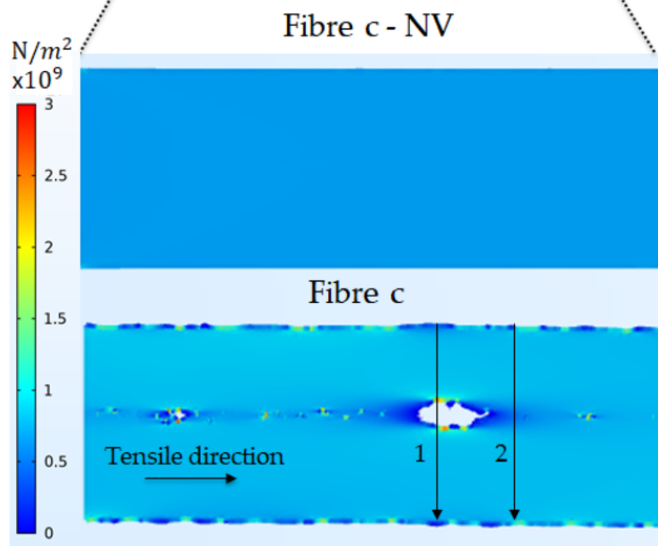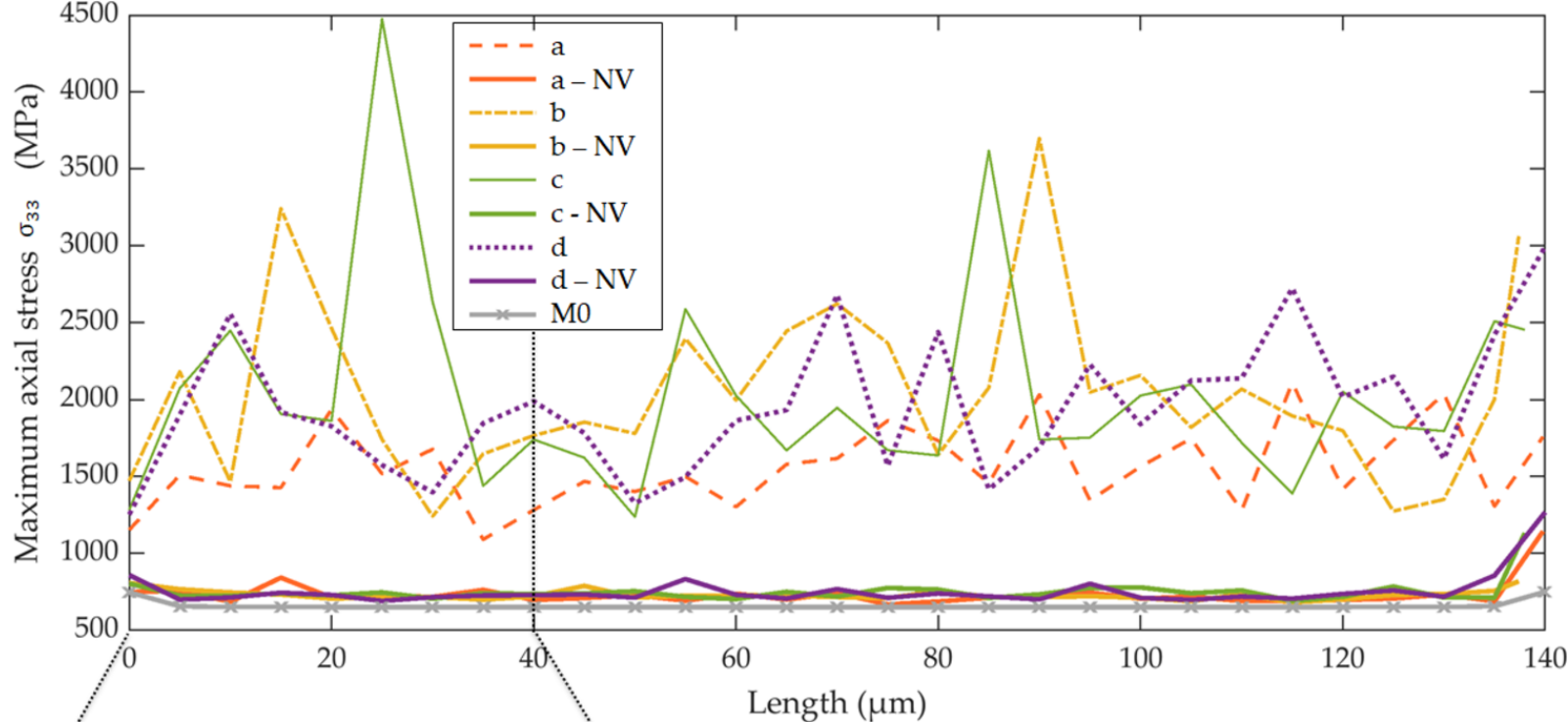
Table captions

Table 1: Summary of samples and related parameters used for the finite element analysis. The fibres a, b, c and d are based on the volumes obtained directly from X-ray tomography. The fibres a-NV, b-NV, c-NV and d-NV were created from the extrusion of the cross-section at one extremity of fibres a, b, c and d respectively. The internal porosity of both fibre types (a, b, c and a-NV, b-NV, c-NV) was removed by image processing leading to the volumes -F and -NV-F respectively. Finally, cylindrical fibres called *fibres models* with a diameter of 15 μm and a lumen content of 0, 1, 3, 5 and 10% are called respectively M0, M1, M3, M5 and M10. As an illustration, fibres a, a-NV, a-F, a-NV-F and M3 are depicted in the table.

Table 2: Aspect ratio, transverse surface area and porosity content of four flax fibres (a, b, c and d) obtained from μ-CT data, with μ the mean value and σ the standard deviation. Last column represents the mean values of the fibres a, b, c, d.

Table 1: Summary of samples and related parameters used for the finite element analysis. The fibres a, b, c and d are based on the volumes directly obtained from X-ray tomography. The fibres a-NV, b-NV, c-NV and d-NV were created from the extrusion of the cross-section at one extremity of fibres a, b, c and d respectively. The internal porosity of both fibre types (a, b, c and a-NV, b-NV, c-NV) was removed by image processing leading to the volumes -F and -NV-F respectively. Finally, cylindrical fibres called *fibres models* with a diameter of 15 μm and a lumen content of 0, 1, 3, 5 and 10% are called respectively M0, M1, M3, M5 and M10. As an illustration, fibres a, a-NV, a-F, a-NV-F and M3 are depicted in the table.
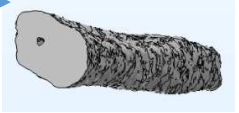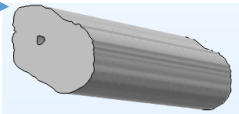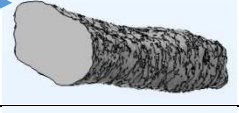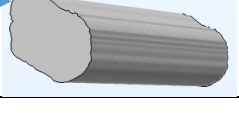
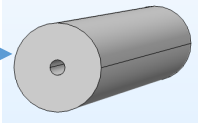| Name	Porosity content (%)	Dof (x10^6)	Mean volume of element (x10^{-3} μm^3)	Variations along fibre length	Typical morphology
a	7.30	2.2	15	X	
b	2.60	4.3	15	X	
c	0.01	4.8	25	X	
d	0	4.2	23	X	
a - NV	0.95	1.1	36		
b - NV	3.53	1.3	49		
c - NV	0.01	1.9	66		
d - NV	0	1.7	55		
a - F	0	1.8	24	X	
b - F	0	2.8	20	X	
c - F	0	3.7	33	X	
a - NV - F	0	0.9	46		
b - NV - F	0	1.0	64		
c - NV - F	0	1.6	81		
M-0	0	0.5	206		
M-1	1	0.7	143		
M-3	3	0.8	129		
M-5	5	0.8	120		
M-10	10	0.7	135		

Table 2: Aspect ratio, transverse surface area and porosity content of four flax fibres (a, b, c and d) obtained from μ-CT data, with μ the mean value and σ the standard deviation. Last column represents the mean values of the fibres a, b, c, d.

Flax sample		Fibre a	Fibre b	Fibre c	Fibre d	Mean
Aspect ratio	μ	**1.48**	**1.26**	**1.04**	**2.07**	**1.46**
	σ	0.17	0.04	0.01	0.12	0.38
Transverse surface area (μm^2)	μ	**54**	**103**	**192**	**145**	**124**
	σ	4.3	4.9	2.5	5	51.0
Porosity (%)	μ	**7.2**	**2.6**	**0.1**	**0**	**2.5**
	σ	4.0	1.1	0.2	0	2.9